Version of Record: https://www.sciencedirect.com/science/article/pii/S1750583621000359
Manuscript_f8aa21c00fb3513f9271bc1b359c1c77

Effect of CO_2-Brine-Rock Reactions on Pore Architecture and Permeability in Dolostone: Implications for CO_2 storage and EOR

Heng Wang[a], Vladimir Alvarado[b,*], Davin A. Bagdonas[a], J. Fred McLaughlin[a], John P. Kaszuba[c,d], Dario Grana[c], Erin Campbell[e], Kam Ng[f]

[a] *Center for Economic Geology Research, University of Wyoming, Laramie, Wyoming, USA*
[b] *Department of Chemical Engineering, University of Wyoming, Laramie, Wyoming, USA*
[c] *Department of Geology & Geophysics, University of Wyoming, Laramie, Wyoming, USA*
[d] *School of Energy Resources, University of Wyoming, Laramie, Wyoming, USA*
[e] *Wyoming State Geological Survey, Laramie, Wyoming, USA*
[f] *Department of Civil & Architectural Engineering, University of Wyoming, Laramie, Wyoming, USA*

Abstract

Geologic carbon sequestration (GCS) is considered a feasible technology for storing substantive volumes of greenhouse gases in subsurface geological formations. In the reservoir, far from carbon dioxide (CO_2) injection wells or in post-injection scenarios, diffusion dominates over advection. This condition conjoins with spatially distributed geochemical reactions to induce heterogeneous changes in pore architecture, i.e. pore body and throat sizes or surface roughness. These changes can affect CO_2 transport properties and storage capacity. In this work, we investigated mineral dissolution and precipitation in dolomite samples saturated with a CO_2-saturated brine at 93 °C and 34.5 MPa, aged without flow. Two rock types samples, i.e. intergranular- and

*Corresponding author
Email address: valvarad@uwyo.edu (Vladimir Alvarado)

Preprint submitted to International Journal of Greenhouse Gas Control February 7, 2021

vuggy-dominant, were selected to investigate changes in pore size, porosity and permeability under reactive conditions. Mineral dissolution and precipitation were characterized using scanning electron microscopy. Changes in pore size were quantified via Time-Domain Nuclear Magnetic resonance (TD-NMR) transverse relaxation time (T_2) and diffusion coefficient (D) distributions. We show that mineral dissolution likely occurs in highly permeable pathways. These observations are confirmed through analysis of (T_2) and diffusion coefficient (D) distributions. In contrast to results during CO_2-enriched brine continuous injection, mineral precipitation was observed in micropores. The leftward shift of the T_2 peaks, corresponding to micropores, also evidenced mineral precipitation in low-permeability zones. However, microscale alterations resulted only in a subtle increase in porosity and permeability. Results in this study shed light on effects of geochemical reactions on alteration of rock properties in diffusion-dominated regions during CO_2 storage.

Keywords: CO_2 storage, Heterogeneous geochemical reactions, Pore structure change, Porosity and permeability change, NMR T_2 and diffusion

1. Introduction

Carbon dioxide (CO_2) emissions from the energy sector powered by fossil fuels have noticeably increased CO_2 concentration in the atmosphere, which has been touted as a significant contributing factor to climate change (Hoffert et al., 2002; Bachu, 2000). Mitigation strategies have been proposed to reduce emissions substantively through safe injection of CO_2 into subsurface reservoirs such as deep saline aquifers (Van der Meer, 1995; Bachu, 2003;

Steele-MacInnis et al., 2012; Liu et al., 2016; Trevisan et al., 2017; Wang et al., 2020), depleted oil/gas reservoirs (Li et al., 2006; Han and McPherson, 2009; Wang et al., 2013; Sun et al., 2016; Olalotiti-Lawal et al., 2019), unminable coal beds (Gale and Freund, 2001; Stauffer et al., 2011; Cao et al., 2020) and oil/gas reservoirs (Shaw and Bachu, 2002; Dai et al., 2013; Tao and Clarens, 2013; Wang et al., 2014; Gong and Gu, 2015; Yu et al., 2020). This strategy is denominated geologic carbon storage (GCS). Among GCS targets, deep carbonate saline aquifers are ideal candidates due to their broad geographical distribution, large storage capacity, and potential long-term storage security (Bruant et al., 2002; Friedmann, 2007; Benson and Cole, 2008). However, carbonate reservoirs are reactive in the presence of CO_2 in the brine. CO_2 dissolution in brine leads to a pH decrease (Kaszuba et al., 2005). In view of the pH drop, understanding of mineral dissolution and precipitation, and the associated changes in static and dynamic properties of rocks, are important considerations for GCS operations.

The impacts of geochemical reactions on pore architecture and petrophysical properties are complex, and they relate to chemical, physical and geological characteristics, such as fluid composition, temperature, pressure, mineralogy and transport properties. In addition, mineral dissolution and precipitation are strongly dependent on the coupling between the local fluid transport and the distribution of dissolved ions. The fate of CO_2 directly relates to the interplay between geochemical reactions and the transport of species within CO_2-enriched formation brine. Of equal importance are the spatial heterogeneity of the pore geometry as well as mineral distribution that result in heterogeneity of the mineral dissolution and precipitation. At

the pore-scale, reactions along mineral boundaries and different associated reaction mechanisms in pores of different sizes, and consequently different surface-to-volume ratios, enable heterogeneous changes in pore structure and properties along flow pathways (Tenthorey and Scholz, 2002; Noiriel et al., 2016; Min et al., 2016; Beckingham, 2017; Luhmann et al., 2017; Adeoye et al., 2017; Noiriel and Deng, 2018). Moreover, changes in fluid composition after reactions in the pore space can give rise to Gibbs free energy gradients, potentially increasing the contrasts in mineral reactivity at various locations, such as pore throats between micro and macropores. Heterogeneous distributions of mineral dissolution and precipitation in the pore space ultimately contribute to changes in pore architecture, i.e. pore shape, pore-size distribution, and mineral reactive surface area. The complex interplay may either widen or clog pores to ultimately impact static and dynamic rock properties, such as porosity, permeability and wettability (Luquot and Gouze, 2009; Sadhukhan et al., 2012; Nogues et al., 2013; Chen et al., 2014; Luhmann et al., 2017; Yee et al., 2018).

Current GCS research using laboratory experiments focuses on investigating changes in porosity and permeability in convective-dominant regions by continuously injecting CO_2-enriched brine, which typically leads to uniform dissolution as the porous medium is surface-reaction controlled (El-Maghraby and Blunt, 2012; Adeoye et al., 2017). For instance, Luquot and Gouze (2009) studied porosity and permeability changes in four zones corresponding to increasing distances from the injection well; these dissolution experiments showed power-law scaling, $k \sim \phi^n$, between permeability and porosity with different values of the n scaling exponents. Regardless of differences in field

injection practices, reservoir regions with convective-dominated transport as well as those with negligible convection arise. As CO_2 injection is interrupted, the convective flow is stopped and transport becomes a rate-limiting process. In this case, reactions are diffusion-dominated. Mass transport between the mineral surface and the pore center, or between micro and macropore spaces are limited, thus leading to poor mixing conditions (Molins, 2015). Heterogeneous pore-scale architecture favors the buildup of the aforementioned local chemical concentration gradients. Overall, localized dissolution and precipitation events occur under these conditions, thus potentially increasing or decreasing the conductivity of specific flow pathways, which in turn drive changes in permeability (Kang et al., 2010). To date, very few research efforts focus on diffusion-dominant zones (shown in Figure 1) and subsequent consequences of limited supply of carbonic acid on petrophysical properties.

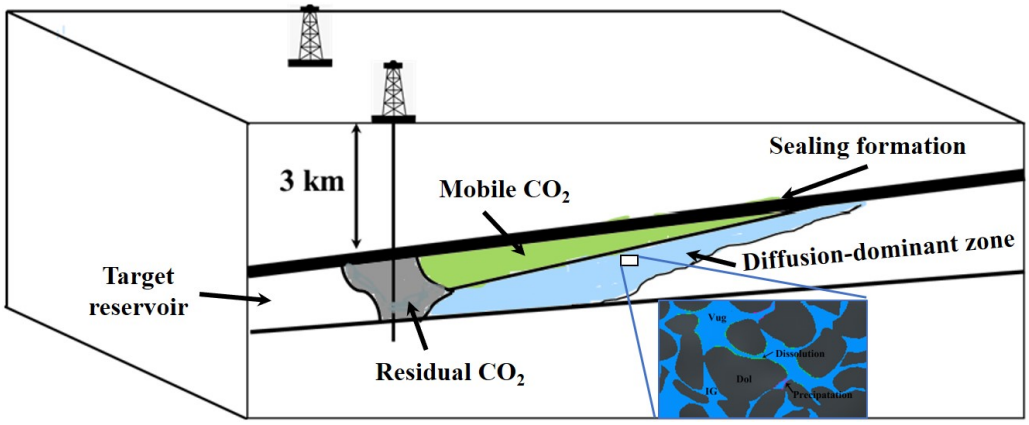

Figure 1: Schematic diagram of CCS/EOR scenario in a subsurface target reservoir. For regions far from injection wells or in post-injection periods, diffusion dominates over advection.

The objective of this study is to investigate complex changes in pore ar-

chitecture, i.e. pore body and pore throat sizes, or surface roughness, and petrophysical properties (i.e. porosity and permeability) caused by the heterogeneous geochemical reactions in the pore space in regions far from carbon dioxide (CO_2) injection wells or during post-injection scenarios. Dolomite samples were collected from the two rock types identified, namely vuggy- and intergranular-dominant porosity in the Madison Limestone, which is located in the Rock Springs Uplift (RSU), Southwestern Wyoming (shown in Figure 2) (Surdam, 2013; Wang et al., 2018). In this research, we investigated changes in pore architecture and their impact on permeability and porosity in two different rock types as driven by mineral dissolution and precipitation in a diffusion-dominated system containing limited carbonic acid. To mimic this condition, the core samples were reacted with stagnant CO_2-enriched brine in a core-flooding apparatus at reservoir conditions (34.5 MPa and 93 °C) for 400 hours. Our results uncover connections between reactivity in diffusion-dominant regions and potential larges-scale effects on storage, as to provide a better understanding of the subsequent dynamics of the multiphase flow system.

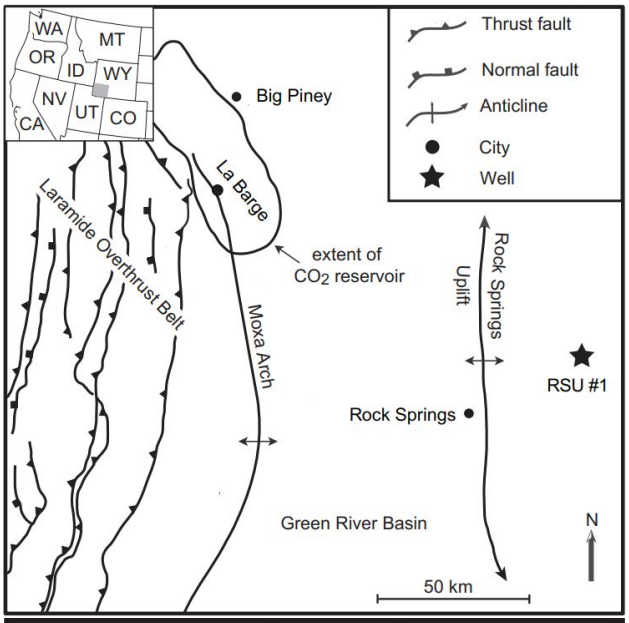

System	Depth	Formation
Jurassic		Nugget Ss
Triassic	3048 m	Chugwater Fm
		Dinwoody Fm
Permian	3353 m	Phosphoria Fm
Pennsylvanian		Weber Ss
	3658 m	Amsden Fm
Mississippian	A B	Madison Ls
Devonian		Darby Fm

Figure 2: Top: Geologic map of Rock Springs Uplift, Southwestern Wyoming, United States, and the location of well RSU #1 where the rock samples were drawn. RSU = Rock Springs Uplift.; Bottom: Stratigraphic column for well Rock Springs Uplift #1 including cored intervals: Madison samples were collected from depth interval A (3766 m) and B (3783 m). Fm = formation; Ss = Sandstone; Ls = Limestone.

2. Experimental Section

2.1. Materials

Brine used in the experiments was prepared based on the chemical composition of the formation brine in the Madison Limestone, as shown in Table 1. The brine was degassed for four hours under vacuum before use in the experiment. A second, CO_2-saturated brine was prepared by equilibrating degassed synthetic brine with CO_2 (99.999% purity) for 24 hours at reservoir conditions (34.5 MPa and 93°C).

Four core plugs (24.3 mm in diameter and 50.0 mm in length) of Madison Limestone recovered from the well RSU#1 were selected for experiments. Two of the four samples (MH1 and MH3) are dominated by vuggy pores and two additional samples (MH2 and MH4) are dominated by intergranular pores (Table 2). All four samples were cleaned in soxhlet extractors using toluene and methanol, and oven-dried at 100°C for 24 hours. Routine core analyses (nitrogen porosity and permeability) were carried out under a net confining pressure of 3.5 MPa using a Coreval 700 permeameter and porosimeter (VINCI Technologies, France). Klinkenberg permeabilities of the core plugs were used to correct nitrogen permeability measured to equivalent liquid permeability. Properties of each sample are summarized in Table 2. Samples prepared for the scanning electron microscope (SEM) and thin section were trimmed from these core plugs. Two addition samples (mini plugs MH5 and MH6: 8 mm in diameter and 10 mm in length) were drilled near the extraction locations of samples MH3 and MH4 for diffusion coefficient measurements.

Table 1: Chemical concentrations of synthesized and produced brine. pH of the degassed synthetic brine is 6.7.

Major Species/Complexes	Concentration, mol/kg
SO4	0.1052
Cl	1.6190
Na	1.4760
K	0.0596
Mg	0.0030
Ca	0.0040

Table 2: Core plug properties before and after reaction. The standard errors of the nitrogen porosity and Klinkenberg permeability are ±0.05% and ±0.5 mD, respectively

Pore-type	Sample #	Depth, m	Porosity, %		Permeability, mD	
			before	after	before	after
Intergranullar	MH1	3765.8	16.22	16.39	14.06	15.27
	MH3	3765.9	19.46	19.66	14.21	16.91
	MH5	3765.9	-	-	-	-
Vuggy	MH2	3782.6	18.16	19.45	65.09	74.90
	MH4	3782.7	16.34	17.26	30.76	40.67
	MH6	3782.7	-	-	-	-

2.2. SEM and Thin Section

Core plugs MH1 and MH2 were evaluated using thin section and scanning electron microscope (SEM) analyses to characterize mineralogy and pore architecture and to identify potential mineral dissolution and precipitation. Selected samples were sent to Wagner Petrographic, Lindon, Utah, for thin section preparation. Most of the thin sections were stained for calcite and feroan carbonates, and impregnated with epoxy for porosity evaluation. SEM analysis was performed using an FEI Quanta FEG 450 field emission scanning electron microscope. Samples were carbon-coated for high-vacuum SEM analysis ($> 10^{-5}$ torr) and backscattered electron images were obtained using a 20 kV electron beam.

2.3. Transverse Relaxation Time (T_2)

^{1}H NMR T_2 relaxation time, also known as transverse relaxation time, can be used to estimate pore-size distribution. For rock samples fully saturated with brine, proton spins relax through three independent relaxation mechanisms: bulk fluid ($T_{2,\ bulk}$), surface ($T_{2,surface}$) and diffusion ($T_{2,diffusion}$). In the fast diffusion regime, the T_2 relaxation can be calculated as (Wang et al., 2018):

$$\frac{1}{T_2} = \frac{1}{T_{2,bulk}} + \frac{1}{T_{2,surface}} + \frac{1}{T_{2,diffusion}} \tag{1}$$

As diffusion relaxation is minimized and bulk relaxation rate is sufficiently small, T_2 is dominated by $T_{2,surface}$. T_2 can then be simplified as (Wang et al., 2018):

$$\frac{1}{T_2} \approx \rho \frac{S}{V_p} \tag{2}$$

where ρ is surface relaxivity; S and V_p are surface area and pore volume, respectively. As the V_p/S ratio is proportional to pore size, the T_2 distribution relates to the pore-size distribution.

The area under the T_2 distribution curve is proportional to the number of hydrogen protons that are contained in the pore fluids within the sensitive volume. The division between different pore sizes using fixed cutoff values is commonly used to separate the bound and free fluid portion in NMR data interpretations. Figure 3 shows an example of T_2 distribution of a core plug (porosity is ϕ) fully saturated with brine. The shortest T_2 represents fluid (A1) that is bounded by clay. The smaller pores, also known as micropores (faster T_2), contain capillary fluid (A2) that is bound by capillary forces and the remaining water film in larger pore surfaces. The largest pores, also known as macropores (the largest T_2), contain free fluid (A3) or fluid that is free to move. The porosity of the larger pores can be calculated as $\phi A3/A$. This method will be used to investigate the change in pore size or its corresponding porosity induced by the mineral dissolution and precipitation. In this study, NMR T_2 measurements of samples MH3 and MH4 before and after reaction were collected using a Bruker BioSpin LF110 instrument at 25°C and atmospheric pressure using a standard Carr-Purcell-Meiboom-Gill (CPMG) pulse sequence.

2.4. Restricted Diffusion Coefficient

The effective diffusion coefficient measured using pulsed field gradient (PFG) NMR has been used to provide a better understanding of fluid trans-

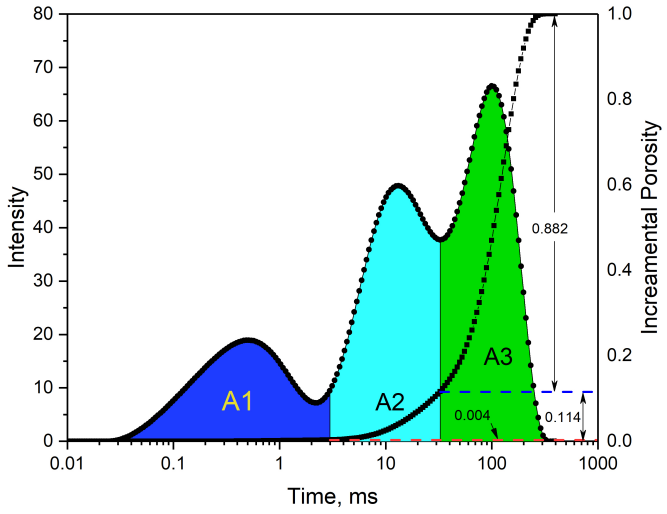

Figure 3: An example of T_2 distribution of a core plug saturated with brine. The porosity of different pore types divided by two cutoff values can be expressed as Ai/A, where Ai is $A1$, $A2$ and $A3$.

port in diffusion-dominant regions and to provide the effective diffusion coefficient spectra (Wang et al., 2018). In the short observation time limit, the root-mean-squared displacement for a fraction of the diffusive water molecules near pore surfaces is reduced compared to the value of the bulk fluid free diffusion. In porous media, hydrogen-bearing molecules exist in a variety of different pore sizes, where the measured signal attenuation is a sum of contributions from all hydrogen spins. As a result of the gradient increase, a deviation of the logarithm of intensity ratio will occur. A non-negative least-square algorithm can be used to fit the diffusion coefficient decay curve and to calculate diffusion coefficient distribution (Wang et al. (2018). The calculated diffusion coefficient distribution not only represents pore-size distribution, but it also provides a hint of molecular diffusive transport in pores of different sizes. In this study, the two mini plugs (MH5 and MH6) were reacted with CO_2-saturated brine inside a transfer vessel at reservoir conditions. NMR diffusion coefficients before and after reaction were determined at a series of gradient strengths to quantify the changes in spatial diffusion coefficient distribution. The diffusion coefficient for the mini plugs were collected using a Bruker BioSpin mq20 instrument with a 10 mm (diameter) $\times$ 10 mm (length) chamber. The pulsed field gradient NMR sequence introduced by Stejskal and Tanner (1965) was selected. In the fast-diffusion regime, the spin echo amplitude is described as:

$$ln\frac{I(g)}{I(0)} = -\gamma^2 g^2 \delta^2 D(\Delta - \frac{\delta}{3}) \tag{3}$$

where δ is the length of a gradient pulse, γ is the proton gyromagnetic ratio, g is the applied gradient strength, and $I(g)$ and $I(0)$ are the amplitude of the

signal after the first radio frequency pulse with and without gradient strength being applied, respectively. The amplitudes of the gradients strengths range from 2.17 to 3.29 T/m, with a total of 30 points collected. Since the diffusion coefficient is sensitive to temperature, a fluid circulator (F12-MA, JULABO USA Inc.) with a temperature accuracy better than ±0.02 °C was used to warm the sample by circulating temperature-constant coolant liquid.

2.5. Geochemical Reaction Experiment

Geochemical reaction experiments were conducted in a high pressure/high temperature core-flooding system, as shown in Figure 4. Core plugs were wrapped with a heat-shrink tube and Viton sleeve before placing them in a coreholder. Synthetic brine was added to fully saturate the core plugs at the start. Upon saturation, the samples were brought up to reservoir conditions (34.5 MPa and 93 °C). High precision syringe pumps (260D, Teledyne ISCO) were used to inject fluids and to maintain the confining and back pressures (pore pressure). Core plugs were first equilibrated with brine at reservoir conditions for 400 hours. CO_2-saturated brine was then injected into the core plug to fully displace the synthetic brine. The core-flooding system was subsequently shut in and the core plug reacted with CO_2-saturated brine for an additional 400 hours.

As the experiment was finished, the core plugs were flushed with 10 pore volumes of deionized water to displace the brine to prevent subsequent salt precipitation. Then, they were further cleaned in soxhlet extractors using toluene and methanol, and oven-dried at 100 °C for 24 hours. The cleaned dry core plugs were used for additional measurement, i.e. gas (N_2) permeability, porosity, and NMR-T_2 distribution to detect potential changes after reaction.

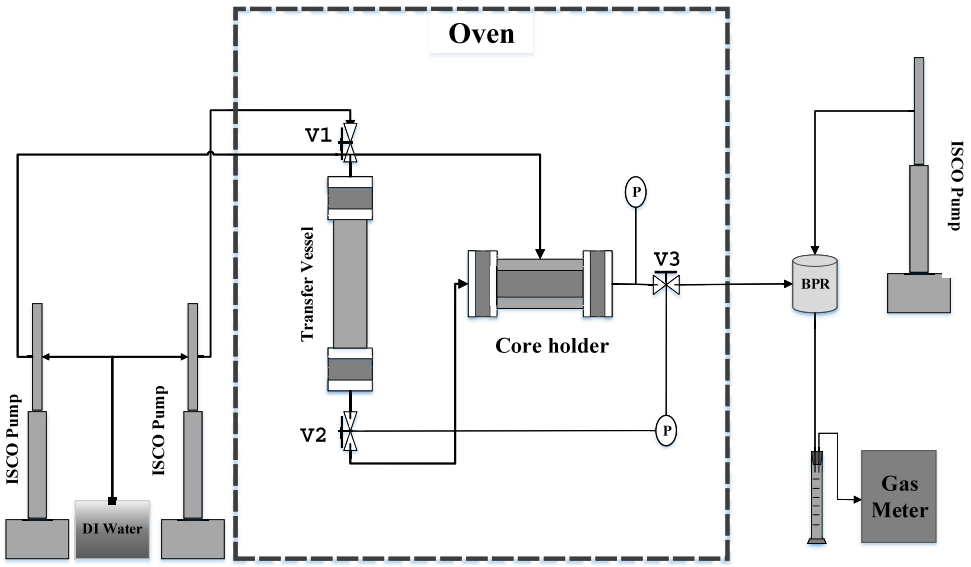

Figure 4: Schematic of coreflooding system used in this study. Once a constant gas production rate is monitored by the gas meter, valves V2 and V3 are closed for stagnant reaction purpose.

Finally, samples were collected from the samples MH1 and MH2 for SEM imaging to detect potential mineral dissolution and precipitation.

3. Experimental Results and Discussion

3.1. Influence of Geochemical Reactions on Porosity and Permeability

The Madison Limestone rock samples exhibit two styles of porosity, namely intergranular-dominant, characterized by a homogeneous pore-size distribution, and vuggy-dominant, characterized by a variable pore-size distribution (McLaughlin et al., 2012, 2013). Examples of the porosity types are shown in Figure 5a. The figure shows a vug that is surrounded by smaller, uniform dolomite grains that typify the reservoir's intergranular porosity system. Though the intergranular pores are smaller, they are evenly distributed and provide the majority of the pore space. For vuggy-dominant pores, vuggy, sometimes moldic, porosity forms by diagenetic dissolution of the carbonate and/or anhydrite (Figure 5b). In addition, small secondary mineral particles of quartz and dolomite up to 10 μm were observed on the surface of primary dolomite and quartz grains.

CO_2-brine-rock reactions can induce mineral dissolution and precipitation to lead to changes in porosity by widening or clogging pore-bodies and pore-throats. Mineral dissolution increases pore volume while precipitation does the opposite. The net change of porosity is determined by the balance between these mechanisms. In this study porosity measured before and after reaction are provided in Table 2. The increments in porosity for MH1 and MH3 (intergranular-dominant samples) are 0.17% and 0.2%, respectively. The small difference mainly results from the finite amount of carbonic acid

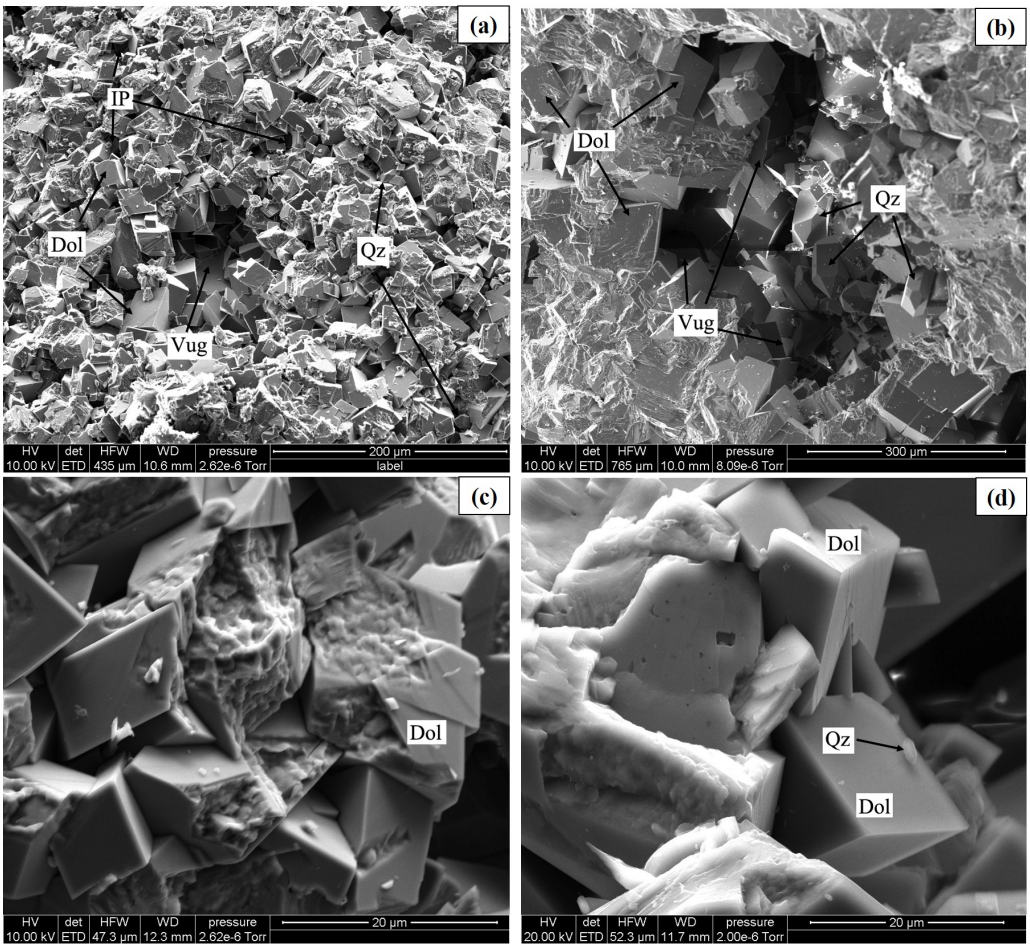

Figure 5: Scanning electron microscope (SEM) of samples MH1 and MH2 prior (a and b) and after (c and d) reaction. (a) MH1: a mixed intergranular and vuggy porosity system. (b) MH2: a dominantly vuggy porosity system. Authigenic quartz crystals have nucleated in vugs. (c) MH1: pitting on the crystal surface and broken crystal faces becomes deeper. (d) MH2: pitting on the crystal surfaces became deeper and small particles on the surface of dolomite crystals are mostly dissolved. Dolomite crystals around vuggy pores become smaller than matrix dolomite grains. Dol: dolomite; Anh: anhydrite; Qz: quartz; IP: intergranular pore.

in the brine and slow reactive-diffusive transport when in contact with the acid brine in the reaction process. As opposed to intergranular-dominant samples, the porosity of vuggy-dominant samples, MH2 and MH4, increased from 18.16 to 19.45% and from 16.34 to 17.26%, respectively. In addition to the chemical reactions, the physical loss of grains and the movement of clay, or dolomite and quartz fine particles might also contribute to the increasing porosity in both samples (Pearce et al., 2016; Dávila et al., 2017; Pearce et al., 2019). Pearce et al. (2019) observed that the changes in porosity calculated from μCT density is less than 0.5% owing to movement of clays or fines. However, McLaughlin et al. (2012) showed that the Madison Limestone contains minor clays and fine particles, which can also be found in the SEM images before the reaction in Figure 5. Therefore, compared with chemical reactions, the porosity increased due to the physical movement of the clays and fine particles is relatively negligible.

Porosity of sample MH1 is comprised mainly of homogeneous intergranular pores. These pores were filled by CO_2-saturated brine and pore walls dissolved uniformly. Negligible dissolution of dolomite occurred (Figure 5 (c)), because of the limited volume of reactive fluids. However, etch pits on mineral surfaces suggest dolomite dissolution. The most prominent dissolution texture within the integranular sample are nascent channel structures with walls of smaller (relative to matrix), partially digested dolomite crystals.

Figure 5 (d) shows an SEM image highlighting vuggy pores. The small mineral particles (dolomite) on the surface of dolomite crystals are mostly dissolved. Pitting of crystal surfaces became deeper after reactions, while dissolution on the edge and corner of dolomite crystals cannot be validated based

solely on the SEM images. Pore systems in sample MH2 are vug-dominated. The displacing reactant fluid mainly flowed along the most highly permeable pathways, suggesting dissolution reactions happen, while in surrounding intergranular pores (matrix), the reactions are limited (Luquot et al., 2014). In addition to the mineral dissolution, mineral precipitation is also observed in both rock samples, shown in Figures 6 and 7. The newly precipitated minerals are located on dolomite crystals in micropores and have a distinctly irregular morphology. The energy dispersive spectra (EDS) of neoformed minerals from two post-reacted samples and from pre-reacted dolomite crystals were collected within red circled area, shown in Figures 6 and 7. Elements such as Ca, C, O, Mg are shown in the EDS spectra of both original dolomite and the neoformed minerals, indicating that the precipitated minerals are chemically similar to the originally present. However, it is hard to determine whether the precipitates are dolomite or a mixture of dolomite and calcite solely from the EDS spectra.

In contrast with changes in porosity after geochemical reactions, permeability evolves non-linearly, which is likely driven by the spatial distribution of reactions in individual pores and pore-throats. In this study, permeability for MH1 and MH3 increased from 14.06 and 14.21 mD to 15.27 and 16.91 mD, respectively. Mineral dissolution, as observed from SEM images shown in Figure 5, increased the smoothness of pore surface, widening the pore body and pore throat along the flow pathways, thus increasing permeability after reaction. Even though porosity of MH1 and MH3 is similar to that of MH2 and MH4, it is somewhat surprising that permeability after reactions increased 1.2 and 1.3 times, respectively, for the latter samples. The incre-

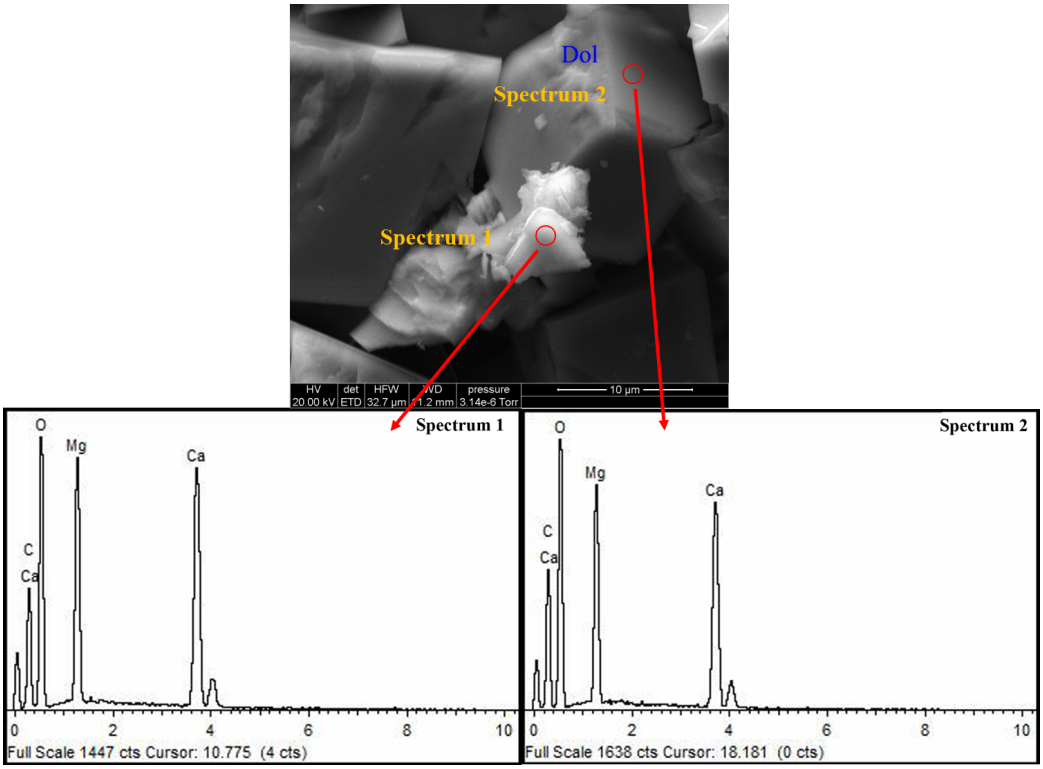

Figure 6: SEM image and EDS spectra (within red circles) of originally and newly precipitated mineral in sample MH1. Comparison of Spectrum 1 (neoformed mineral) to host dolomite(Spectrum 2) shows that the newly precipitated minerals are chemically similar to original dolomite. Dol: dolomite.

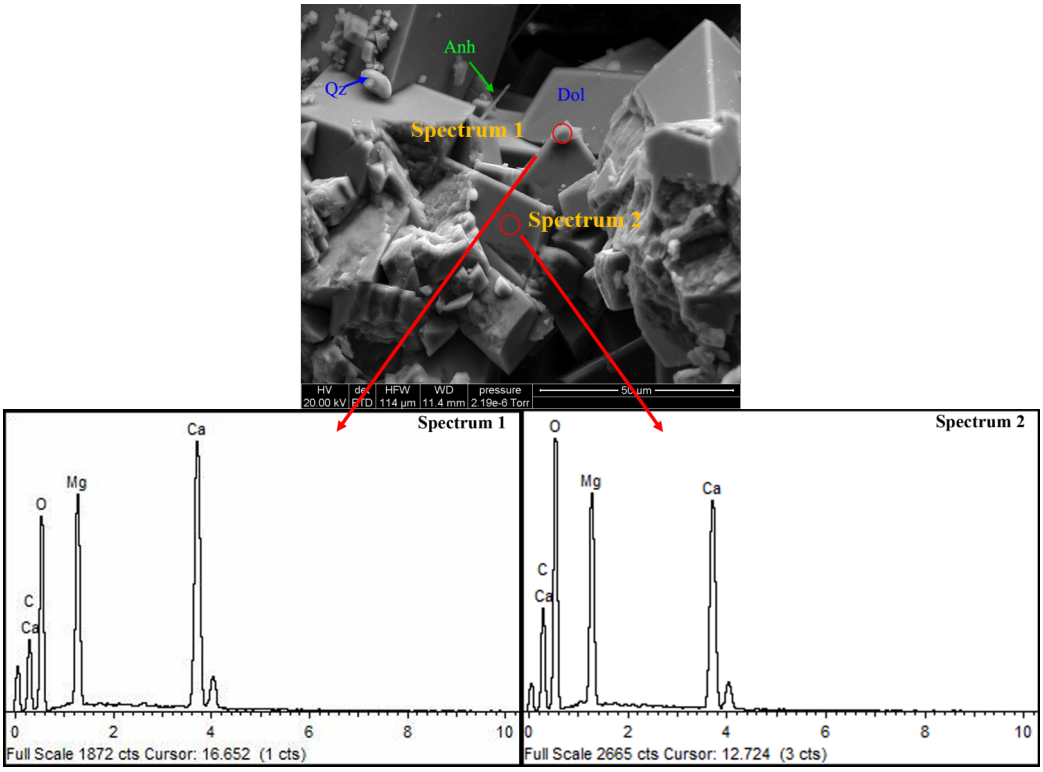

Figure 7: SEM image and EDS spectra (within red circles) of originally and newly precipitated minerals in sample MH2. Comparison of Spectrum 1 (neoformed mineral) to host dolomite (Spectrum 2) show that the newly precipitated minerals are chemically similar to original dolomite. Dol: dolomite; Qz: quartz; Anh: anhydrite.

ment of permeability are likely induced predominantly by pore-throat size alteration, especially for the smaller pore throats along the flow pathways (Luhmann et al., 2017). Irreversible geochemical changes may occur, such as creating new flow pathways, which has a significant influence on permeability (Rutqvist, 2012). The changes in pore size that mostly relates to pore-throat size can be recorded from the NMR T_2 and effective diffusion coefficient distributions, which will be discussed in the following sections.

3.2. NMR T_2 Distribution

Pore size changes due to mineral dissolution and precipitation can be determined from T_2 distributions of hydrogen nuclei, in which the longer T_2 values correspond to smaller surface area-to-volume ratio, thus larger pores. The transverse relaxation for the two type samples shows different responses. In Figure 8 (A), two peaks with a shorter T_2 peak and a longer T_2 peak are shown in the T_2 distribution of MH3, representing micro and intergranular pores, respectively. As the porosity of sample MH3 is dominated by intergranular pores, the area under the longer T_2 peak is much larger compared to the porosity of micropores. The T_2 of the rightmost peak that corresponds to larger intergranular pores increases from 65.3 to 67.1 ms after reaction, suggesting mineral dissolution in the intergranular pores. As for micropores, decrease of T_2 for the leftmost peak after reaction is observed, indicating the pore size decreases in micropores, because of mineral precipitation. In addition, the porosity fractions of MH3 are calculated from T_2 distributions, as shown in Figure 9 (A). After reaction, the incremental porosity of intergranular pores increased from 0.987 to 0.989, and the corresponding porosity increased from 19.22% to 19.45%.

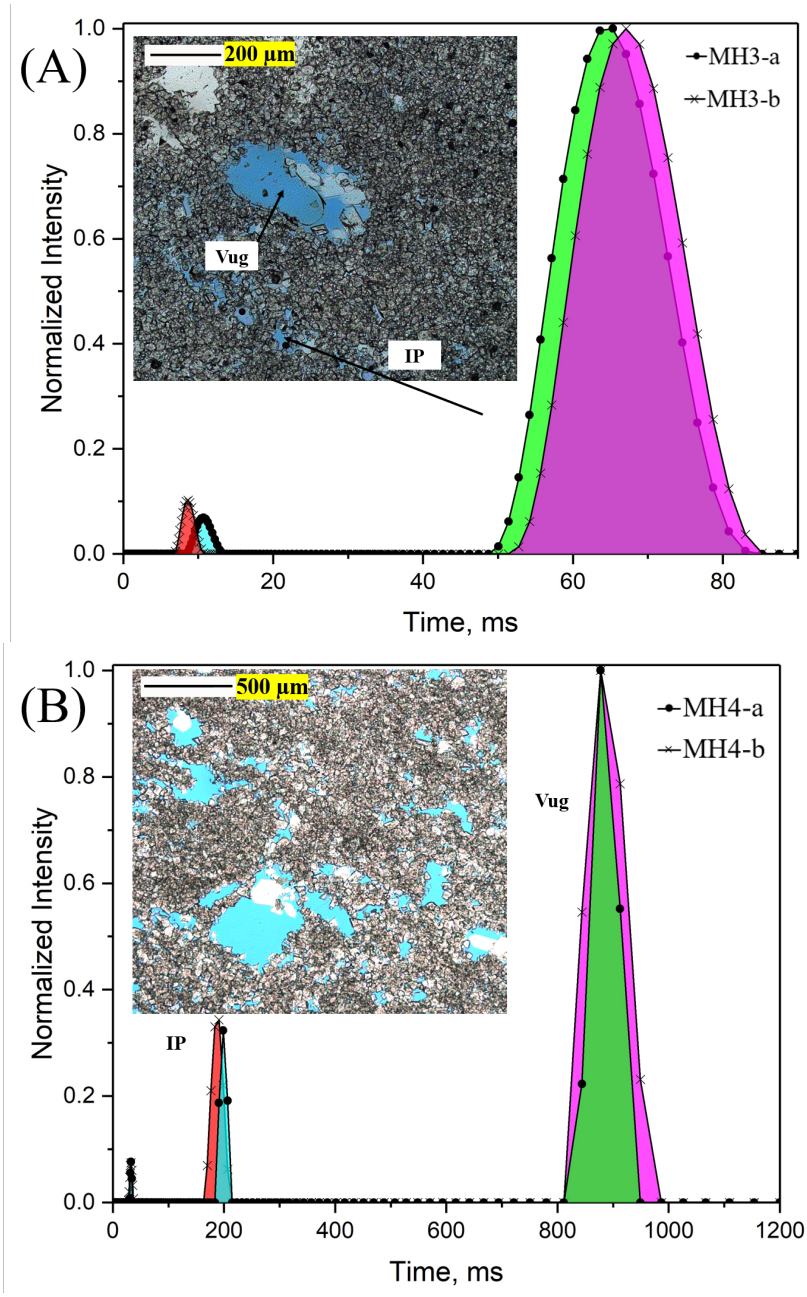

Figure 8: NMR T_2 distributions of MH3 (A) and MH4 (B) prior and post reacting with CO_2-enriched brine. a: prior reaction; b: after reaction. Thin section images before reaction shown with the T_2 distributions are used to clearly link the peaks to the pores.

In contrast with sample MH3, mineral dissolution and precipitation are complex for vug-dominant porous media, especially for the intergranular pores. Figure 8 (B) shows three peaks corresponding to micropores, intergranular pores and vugs from left to right for sample MH4. Shifts of the dominant peak are not recorded for the rightmost peak (vugs) after reaction. However, the T_2 spectrum of vugs becomes wider because of mineral dissolution. Porosity of the vuggy pores calculated from the porosity fractions (shown in Figure 9 (B)), increased from 14.95% to 15.62%. T_2 representing intergranular pores after reaction in sample MH4, decreases from 198.5 to 190.1 ms due to mineral precipitation. Similar findings were observed from pore radii distribution calculated from mercury intrusion capillary pressure curves. Wang et al. (2020) observed that for micropores ranging from 0.2 to 1 μm, the porosity fraction decreases after reaction due to mineral precipitation that clogs these pores or their accessibility. For intergranular pores, permeability is controlled by the micropores or small pore throats, their content is unlikely displaced by CO_2-enriched brine. Besides, minerals are likely to dissolve in the intergranular pores that are connected to vugs along the high permeable pathways. However, these dissolution should not be interpreted directly and singly from changes in the T_2 peaks position. The evidence of dissolution can be inferred from the fact that the porosity of the intergranular pores increased from 1.32% to 1.59%.

Pore-size distribution analysis via T_2 distribution together with texture analysis indicate that the heterogeneity of the pore structure has a significant effect on dissolution and precipitation events. Mineral precipitation is favored in zones of reduced fluid transport, such as micropores for samples

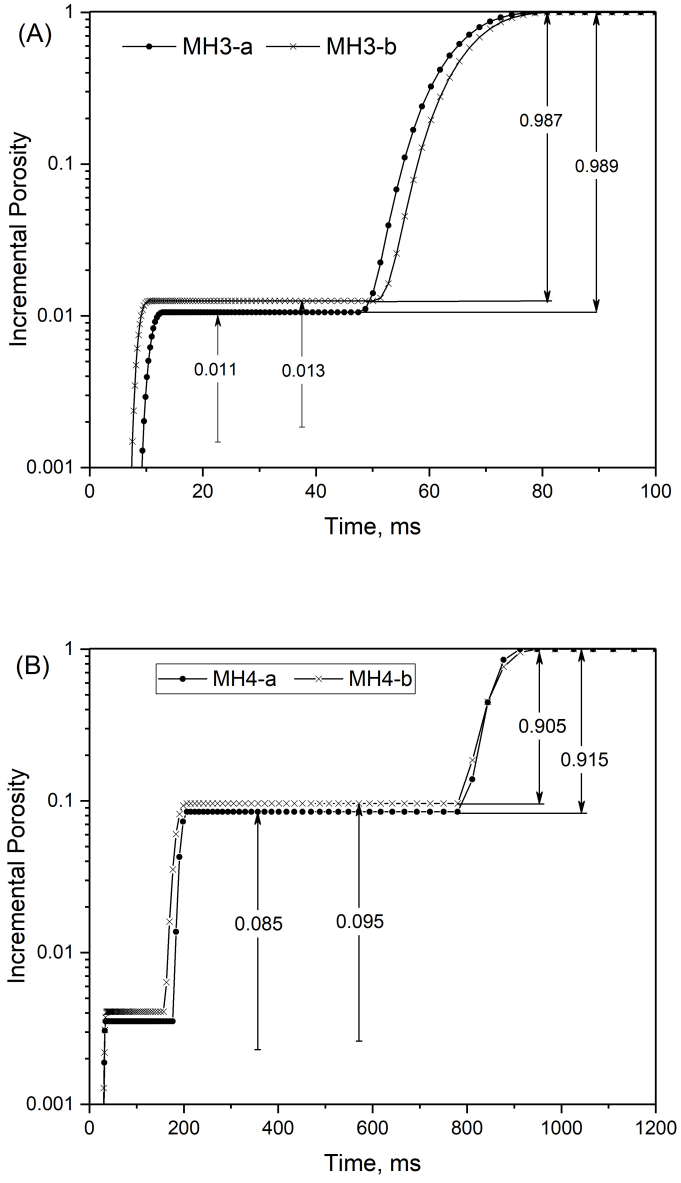

Figure 9: Incremental porosity calculated from T_2 distribution for samples MH3 (A) and MH4 (B) prior and post reacting with CO_2-enriched brine. Porosity fraction under the peaks from left to right for sample MH3 prior and post reaction are 0.013, 0.987 and 0.011, 0.989, respectively. For sample MH4, porosity fraction under the rightmost peaks decreased from 0.915 to 0.905.

MH1 and MH3 and micro/intergranular pores for samples MH2 and MH4, where chemical gradients are small and likely facilitate localized supersaturation of the fluid and increase of pH (Andreani et al., 2009). In contrast, larger chemical gradients develop at the mineral/fluid interface in larger pores, in which molecular transport is more active. In addition, viscosity differences between CO_2-saturated brine and displaced brine might also favor a heterogeneous distribution of reactions. The viscosity of CO_2-saturated brine is less than that of the displaced brine at reservoir conditions (Duan and Sun, 2003; Islam and Carlson, 2012; McBride-Wright et al., 2014). CO_2-saturated brine may preferentially percolate through high permeable pathways, i.e. intergranular pore and vugs in samples MH3 and MH4, respectively. Thus, after brine displacement was stopped, CO_2-enriched brine was located mainly in larger pores, while the CO_2 concentration of brine in small pores was low or could be ignored. In diffusion-dominated reactions where carbonic acid is introduced into the system, dolomite dissolution took place within pore throats and larger pores. Mineral dissolution may have subsequently enlarged the size of pore throats and large pores, and increased calcium and magnesium ion concentrations. Aqueous calcium and magnesium in large pores might migrate to smaller pores (micropores for MH3 and intergranular pores for MH4) driven by concentration gradients, which are controlled by static properties such as pore structure and molecular transport properties such as diffusion. Within smaller pores, those with poor fluid transport properties, mineral precipitation becomes dominant because of fluid super saturation with respect to calcite and dolomite. This precipitation occurs while minerals dissolve in larger pores with greater potential for fluid flow.

In addition, within micropores containing fluid supersaturated with respect to calcite and dolomite, small particles on the surface of dolomite crystals are difficult to dissolve and might serve as effective nucleation sites (Noiriel et al., 2016), thus decreasing the size of smaller pores.

3.3. Effective Diffusion Coefficient Distributions

Molecules and ions diffuse in the restricted pore space representing a complex transport mechanism that affects dissolved CO_2 transport as well as the heterogeneous distribution of different reactions under stagnant fluid conditions. In contrast with the four core plugs that contact the reactant fluid inside a core-holder, samples MH5 and MH6 were submerged in CO_2-enriched brine. The effective diffusion coefficient of hydrogen-carrying molecules measured by the PFG-NMR method provides information on dynamic transport properties in the restricted pore space.

The average diffusion coefficient of water molecules in a pore measured by PFG-NMR is dependent on observation time and surface area-to-pore volume ratio (inversely proportional to pore size). At short observation times, the mean squared displacement for effective diffusion is significantly smaller than the average pore size and only a small fraction of the water molecules can reach the restricting surface. In this study, the observation time is set a constant, thus the measured diffusion coefficient is proportional to the average pore size. At the same gradient strength, the effective diffusion coefficient of both samples increased after the reaction process, shown in Figure 10. As temperature and brine chemistry are the same during all measurements, increased effective diffusion coefficient values provide an indicator of the mineral dissolution (Wang and Alvarado, 2018).

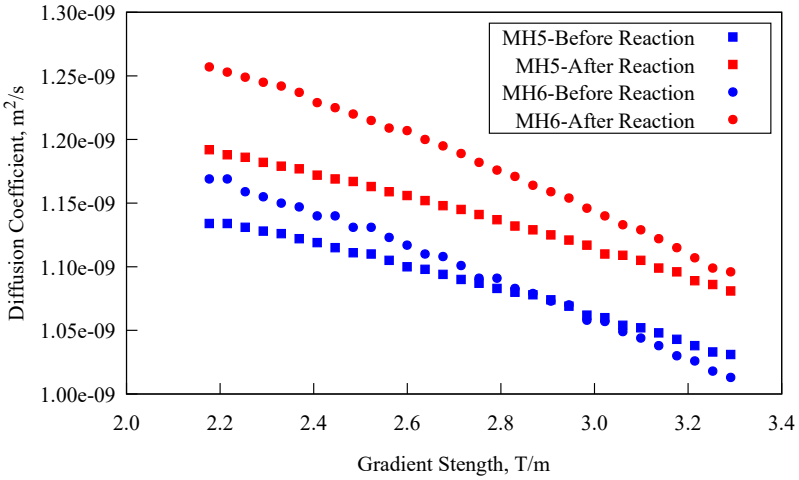

Figure 10: Effective diffusion coefficient decay of samples MH5 and MH6 before and after reaction.

From our previous work, the spatial distribution of the effective diffusion coefficient can be determined by the non-negative least-square method (Wang et al., 2018). Unlike T_2 distributions that are bimodal, the effective diffusion coefficient distribution before reactions for MH5 shows unimodal distributions (Figure 11). The difference in the number of modes is because the pore volume of the mini plugs is small, and the signal from micro pores, where the pore volume is much smaller compared to the pore volume of intergranular pores, is too weak to be captured by the probe. However, a small peak emerged after reaction because of the increase of pore volume in pore throats or micropores due to mineral dissolution. Moreover, the effective diffusion coefficient value at the dominant peak increased because of the increase in the pore size of intergranular pores, which agrees with changes in the T_2 distribution. Sample MH6 yielded two T_2 peaks, which we associated with macro and intergranular pores. The small peak shows that the pore

volume of intergranular pores is small compared with macro-pore volume.

The spatial distribution of the effective diffusion coefficient for samples MH5 and MH6 provides an indication of heterogeneity of reactive transport. Effective diffusion coefficients of cations (like calcium and magnesium) and molecules in macro-pores lead to transport of cations and molecules to micropores as driven by the concentration gradient as well as random translational motion (Stepišnik, 1993). Preferential diffusion likely accelerates mineral precipitation within smaller pores and pore throats between micro and macropores. These smaller pore throats and micropores decrease in size by way of mineral precipitation. However, because of the relatively small pore volume of micropores, an equilibrium might be reached as the concentration gradient decreases, which would slow down the diffusion of calcium and magnesium in response to the corresponding mineral precipitation.

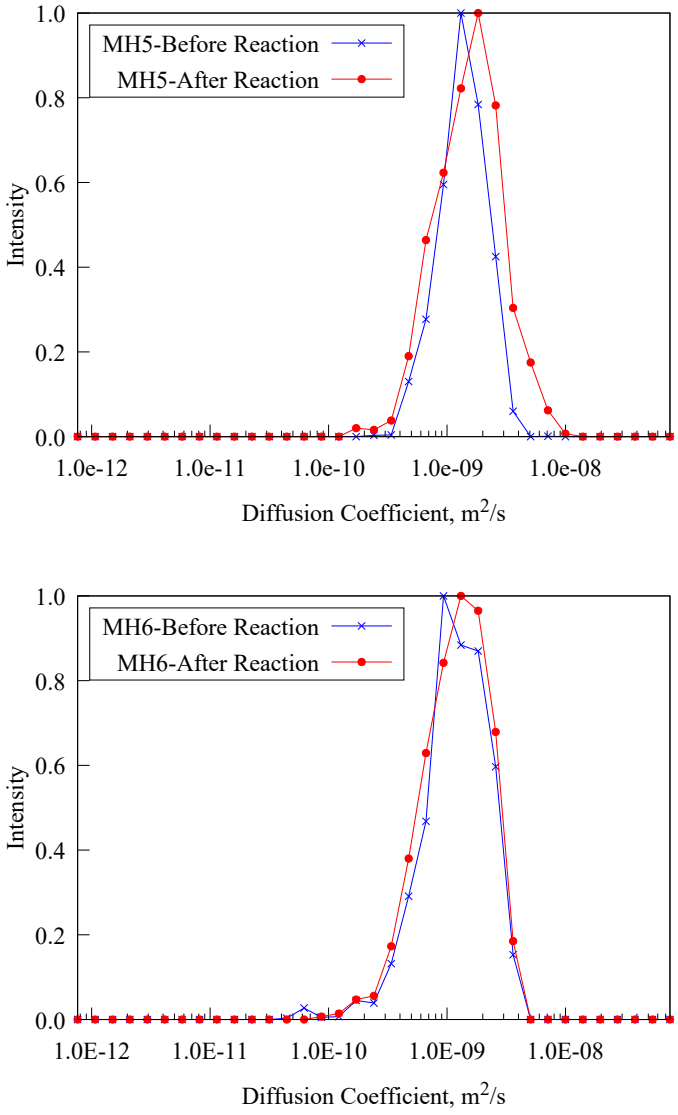

Figure 11: NMR diffusion coefficient distributions of mini plugs before and after reaction under stagnant conditions.

4. Conclusions and Implications

In this study, we focused on how porosity and permeability respond to pore structure and petrophysical property changes for two rock types, as well as the impact of heterogeneity of mineral dissolution and precipitation during CO_2-enriched brine reaction experiments in the absence of flow. Two types of dolomite samples (intergranular- and vuggy-dominant) were reacted with stagnant CO_2-saturated brine at reservoir conditions (93 °C and 34.5 MPa) for approximately 400 hrs. After stagnant reactions, SEM imaging analyses show mineral dissolution in intergranular pores for the intergranular-dominant core sample, and in intergranular and vugy pores for the vuggy-dominant core sample. As opposed to the reported outcome of continuous injection of CO_2-enriched brine, mineral precipitations were observed in micropore spaces. These observations are further confirmed by the shift of peak values for the different pore types from the T_2 and diffusion coefficient distributions. For MH3, the location of the peak that corresponds to the intergranular pores shifts from 65.3 to 67.1 ms, while for micropores, decrease of T_2 values after reaction is observed. For sample MH4, the T_2 peak corresponding to vugs becomes wider after reaction, and T_2 representing intergranular pores after reaction decreases from 198.5 to 190.1 ms due to mineral precipitation. Even though the volume of the reactive carbonic acid is limited as no continuous flow happened, the comprehensive contributions of the heterogeneous reactions are the subtle increase of porosity and permeability.

The spatial heterogeneity of mineral dissolution and precipitation as CO_2-enriched brine is introduced has a great effect on pore structure, especially

for pore throat size, thus changing rock porosity and permeability, with implications for CO_2 plume propagation and storage capacity. For example, the increased permeability favors fluid flow in porous media, which in turn has the ability to increase CO_2 mobility. In contrast, this rock alteration could lower CO_2 sweep efficiency, especially for heterogeneous formations as pore throats increase in high-permeability pathways and decrease in low-permeability pathways. It is important to note that our experimental conditions are representative of a significant portion of the pore space in the subsurface, namely that transport will be diffusion-dominant away from fluid sinks or sources, particularly after injection comes to a halt. Thus, experimental results in this study provide fundamental understanding on effects of geochemical reactions on alteration of rock physical properties and subsequent dynamics of the multiphase flow system. Consequently, a necessary progression of this study should include investigation on how pore structure changes in terms of mineralogy, roughness of pore surfaces and pore throat size by heterogeneous mineral dissolution and precipitation events. The importance of this analysis relates to understanding how reactions can affect the dynamic properties associated with CO_2 such as wettability, relative permeability and capillary pressure. Changes in these crucial properties may in turn affect multi-phase flow that initiates at the pore scale, hysteresis of drainage and imbibition processes, and capillary trapping. This could have a significant influence on the efficiency of capillary pressure trapping, CO_2 plume size and storage capacity. During CO_2 EOR projects, the incremental oil recovery may be affected as well.

Acknowledgment

The authors thanks the Department of Energy for funding through the grant DE-FE0023328. This manuscript is the result of work sponsored by an agency of the United States Government. Neither the United States Government nor any agency thereof, nor any of their employees, makes any warranty, express or implied, or assumes any legal liability or responsibility for the accuracy, completeness, or usefulness of any information, apparatus, product, or process disclosed, or represents that its use would not infringe privately owned rights. Reference herein to any specific commercial product, process, or service by trade name, trademark, manufacturer, or otherwise does not necessarily constitute or imply its endorsement, recommendation, or favoring by the United States Government or any agency thereof. The views and opinions of authors expressed herein do not necessarily state or reflect those of the United States Government or any agency thereof. Kaszuba was supported by the University of Wyoming School of Energy Resources and a Nielson Energy Fellowship.

Adeoye, J.T., Menefee, A.H., Xiong, W., Wells, R.K., Skemer, P., Giammar, D.E., Ellis, B.R., 2017. Effect of transport limitations and fluid properties on reaction products in fractures of unaltered and serpentinized basalt exposed to high P_{CO2} fluids. International Journal of Greenhouse Gas Control 63, 310–320.

Andreani, M., Luquot, L., Gouze, P., Godard, M., Hoise, E., Gibert, B., 2009. Experimental study of carbon sequestration reactions controlled

by the percolation of CO_2-rich brine through peridotites. Environmental Science & Technology 43, 1226–1231.

Bachu, S., 2000. Sequestration of CO_2 in geological media: criteria and approach for site selection in response to climate change. Energy conversion and management 41, 953–970.

Bachu, S., 2003. Screening and ranking of sedimentary basins for sequestration of CO_2 in geological media in response to climate change. Environmental Geology 44, 277–289.

Beckingham, L.E., 2017. Evaluation of macroscopic porosity-permeability relationships in heterogeneous mineral dissolution and precipitation scenarios. Water Resources Research 53, 10217–10230.

Benson, S.M., Cole, D.R., 2008. CO_2 sequestration in deep sedimentary formations. Elements 4, 325–331.

Bruant, R., Guswa, A., Celia, M., Peters, C., 2002. Safe storage of CO_2 in deep saline aquifers. Environmental Science & Technology 36, 240A–245A.

Cao, Z., Deng, J., Zhou, S., He, Y., 2020. Research on the feasibility of compressed carbon dioxide energy storage system with underground sequestration in antiquated mine goaf. Energy Conversion and Management 211, 112788.

Chen, L., Kang, Q., Viswanathan, H.S., Tao, W.Q., 2014. Pore-scale study of dissolution-induced changes in hydrologic properties of rocks with binary minerals. Water Resources Research 50, 9343–9365.

Dai, Z., Middleton, R., Viswanathan, H., Fessenden-Rahn, J., Bauman, J., Pawar, R., Lee, S.Y., McPherson, B., 2013. An integrated framework for optimizing CO_2 sequestration and enhanced oil recovery. Environmental Science & Technology Letters 1, 49–54.

Dávila, G., Cama, J., Luquot, L., Soler, J.M., Ayora, C., 2017. Experimental and modeling study of the interaction between a crushed marl caprock and CO_2-rich solutions under different pressure and temperature conditions. Chemical Geology 448, 26–42.

Duan, Z., Sun, R., 2003. An improved model calculating CO_2 solubility in pure water and aqueous NaCl solutions from 273 to 533 K and from 0 to 2000 bar. Chemical Geology 193, 257–271.

El-Maghraby, R.M., Blunt, M.J., 2012. Residual CO_2 trapping in indiana limestone. Environmental Science & Technology 47, 227–233.

Friedmann, S.J., 2007. Geological carbon dioxide sequestration. Elements 3, 179–184.

Gale, J., Freund, P., 2001. Coal-bed methane enhancement with CO_2 sequestration worldwide potential. Environmental Geosciences 8, 210–217.

Gong, Y., Gu, Y., 2015. Miscible CO_2 simultaneous water-and-gas (CO_2-swag) injection in the bakken formation. Energy & Fuels 29, 5655–5665.

Han, W.S., McPherson, B.J., 2009. Optimizing geologic CO_2 sequestration by injection in deep saline formations below oil reservoirs. Energy conversion and management 50, 2570–2582.

Hoffert, M.I., Caldeira, K., Benford, G., Criswell, D.R., Green, C., Herzog, H., Jain, A.K., Kheshgi, H.S., Lackner, K.S., Lewis, J.S., 2002. Advanced technology paths to global climate stability: energy for a greenhouse planet. Science 298, 981–987.

Islam, A.W., Carlson, E.S., 2012. Viscosity models and effects of dissolved CO_2. Energy & Fuels 26, 5330–5336.

Kang, Q., Lichtner, P.C., Viswanathan, H.S., Abdel-Fattah, A.I., 2010. Pore scale modeling of reactive transport involved in geologic CO_2 sequestration. Transport in Porous Media 82, 197–213.

Kaszuba, J.P., Janecky, D.R., Snow, M.G., 2005. Experimental evaluation of mixed fluid reactions between supercritical carbon dioxide and NaCl brine: Relevance to the integrity of a geologic carbon repository. Chemical Geology 217, 277–293.

Li, Z., Dong, M., Li, S., Huang, S., 2006. CO_2 sequestration in depleted oil and gas reservoirscaprock characterization and storage capacity. Energy Conversion and Management 47, 1372–1382.

Liu, H., He, Q., Borgia, A., Pan, L., Oldenburg, C.M., 2016. Thermodynamic analysis of a compressed carbon dioxide energy storage system using two saline aquifers at different depths as storage reservoirs. Energy conversion and management 127, 149–159.

Luhmann, A.J., Tutolo, B.M., Bagley, B.C., Mildner, D.F., Seyfried, W.E., Saar, M.O., 2017. Permeability, porosity, and mineral surface area changes

in basalt cores induced by reactive transport of CO_2-rich brine. Water Resources Research 53, 1908–1927.

Luquot, L., Gouze, P., 2009. Experimental determination of porosity and permeability changes induced by injection of CO_2 into carbonate rocks. Chemical Geology 265, 148–159.

Luquot, L., Rodriguez, O., Gouze, P., 2014. Experimental characterization of porosity structure and transport property changes in limestone undergoing different dissolution regimes. Transport in Porous Media 101, 507–532.

McBride-Wright, M., Maitland, G.C., Trusler, J.M., 2014. Viscosity and density of aqueous solutions of carbon dioxide at temperatures from (274 to 449) K and at pressures up to 100 MPa. Journal of Chemical & Engineering Data 60, 171–180.

McLaughlin, J.F., Bentley, R.D., Quillinan, S.A., 2013. Regional geologic history, CO_2 source inventory, and groundwater risk assessment of a potential CO_2 sequestration site on the rock springs uplift in southwest wyoming, in: Geological CO_2 Storage Characterization. Springer, pp. 33–54.

McLaughlin, J.F., Quillinan, S., Surdam, R., 2012. Characterizing diagenesis and its opposing impacts on porosity in the weber and madison formations in southwest wyoming: Applying geochemical, petrographic, and isotopic analysis to describe reservoir heterogeneity in potential CO_2 storage sites, in: 2012 GSA Annual Meeting in Charlotte.

Van der Meer, L., 1995. The CO_2 storage efficiency of aquifers. Energy conversion and management 36, 513–518.

Min, T., Gao, Y.M., Chen, L., Kang, Q.J., Tao, W.Q., 2016. Changes in porosity, permeability and surface area during rock dissolution: Effects of mineralogical heterogeneity. International Journal of Heat and Mass Transfer 103, 900–913. URL: <Go to ISI>://WOS:000384777800083, doi:10.1016/j.ijheatmasstransfer.2016.07.043.

Molins, S., 2015. Reactive interfaces in direct numerical simulation of pore-scale processes. Reviews in Mineralogy and Geochemistry 80, 461–481.

Nogues, J.P., Fitts, J.P., Celia, M.A., Peters, C.A., 2013. Permeability evolution due to dissolution and precipitation of carbonates using reactive transport modeling in pore networks. Water Resources Research 49, 6006–6021.

Noiriel, C., Deng, H., 2018. Evolution of planar fractures in limestone: The role of flow rate, mineral heterogeneity and local transport processes. Chemical Geology 497, 100–114.

Noiriel, C., Steefel, C.I., Yang, L., Bernard, D., 2016. Effects of pore-scale precipitation on permeability and flow. Advances in Water Resources 95, 125–137.

Olalotiti-Lawal, F., Onishi, T., Kim, H., Datta-Gupta, A., Fujita, Y., Hagiwara, K., 2019. Post-combustion carbon dioxide enhanced-oil-recovery development in a mature oil field: model calibration using a hierarchical approach. SPE Reservoir Evaluation & Engineering doi:doi:10.2118/187116-PA.

589 Pearce, J., Dawson, G., Golab, A., Knuefing, L., Sommacal, S., Rudolph,
590 V., Golding, S., 2019. A combined geochemical and μct study on the CO_2
591 reactivity of surat basin reservoir and cap-rock cores: porosity changes,
592 mineral dissolution and fines migration. International Journal of Green-
593 house Gas Control 80, 10–24.

594 Pearce, J.K., Golab, A., Dawson, G.K., Knuefing, L., Goodwin, C., Golding,
595 S.D., 2016. Mineralogical controls on porosity and water chemistry during
596 O_2-SO_2-CO_2 reaction of CO_2 storage reservoir and cap-rock core. Applied
597 Geochemistry 75, 152–168.

598 Rutqvist, J., 2012. The geomechanics of CO_2 storage in deep sedimentary
599 formations. Geotechnical and Geological Engineering 30, 525–551.

600 Sadhukhan, S., Gouze, P., Dutta, T., 2012. Porosity and permeability
601 changes in sedimentary rocks induced by injection of reactive fluid: A
602 simulation model. Journal of Hydrology 450, 134–139.

603 Shaw, J., Bachu, S., 2002. Screening, evaluation, and ranking of oil reservoirs
604 suitable for CO_2-flood eor and carbon dioxide sequestration. Journal of
605 Canadian Petroleum Technology 41.

606 Stauffer, P.H., Keating, G.N., Middleton, R.S., Viswanathan, H.S., Berch-
607 told, K.A., Singh, R.P., Pawar, R.J., Mancino, A., 2011. Greening coal:
608 Breakthroughs and challenges in carbon capture and storage. Environ-
609 mental Science & Technology 45, 8597–8604.

610 Steele-MacInnis, M., Capobianco, R.M., Dilmore, R., Goodman, A., Guthrie,

611 G., Rimstidt, J.D., Bodnar, R.J., 2012. Volumetrics of CO_2 storage in deep
612 saline formations. Environmental Science & Technology 47, 79–86.

613 Stejskal, E.O., Tanner, J.E., 1965. Spin diffusion measurements: spin echoes
614 in the presence of a time-dependent field gradient. The Journal of Chemical
615 Physics 42, 288–292.

616 Stepišnik, J., 1993. Time-dependent self-diffusion by NMR spin-echo. Phys-
617 ica B: Condensed Matter 183, 343–350.

618 Sun, D., Ripmeester, J., Englezos, P., 2016. Phase equilibria for the
619 $CO_2/CH_4/N_2/H_2O$ system in the hydrate region under conditions relevant
620 to storage of CO_2 in depleted natural gas reservoirs. Journal of Chemical
621 & Engineering Data 61, 4061–4067.

622 Surdam, R.C., 2013. Geological CO_2 storage characterization: The key to
623 deploying clean fossil energy technology. Springer Science & Business Me-
624 dia.

625 Tao, Z., Clarens, A., 2013. Estimating the carbon sequestration capacity of
626 shale formations using methane production rates. Environmental Science
627 & Technology 47, 11318–11325.

628 Tenthorey, E., Scholz, C.H., 2002. Mapping secondary mineral formation in
629 porous media using heavy metal tracers. Journal of Geophysical Research:
630 Solid Earth 107.

631 Trevisan, L., Pini, R., Cihan, A., Birkholzer, J.T., Zhou, Q., González-
632 Nicolás, A., Illangasekare, T.H., 2017. Imaging and quantification of

633 spreading and trapping of carbon dioxide in saline aquifers using meter-
634 scale laboratory experiments. Water Resources Research 53, 485–502.

635 Wang, H., Alvarado, V., 2018. Ionic strength-dependent pre-asymptoic dif-
636 fusion coefficient distribution in porous media-determination through the
637 pulsed field gradient technique. Journal of Natural Gas Science and Engi-
638 neering 49, 250–259.

639 Wang, H., Alvarado, V., McLaughlin, J.F., Bagdonas, D.A., Kaszuba, J.P.,
640 Campbell, E., Grana, D., 2018. Low-field nuclear magnetic resonance
641 characterization of carbonate and sandstone reservoirs from rock spring
642 uplift of wyoming. Journal of Geophysical Research: Solid Earth 123,
643 7444–7460. doi:10.1029/2018jb015779.

644 Wang, H., Alvarado, V., Smith, E.R., Kaszuba, J.P., Bagdonas, D.A.,
645 McLaughlin, J.F., Quillinan, S.A., 2020. Link between CO_2-induced wet-
646 tability and pore architecture alteration. Geophysical Research Letters 47,
647 e2020GL088490.

648 Wang, H., Liao, X., Dou, X., Shang, B., Ye, H., Zhao, D., Liao, C., Chen, X.,
649 2014. Potential evaluation of CO_2 sequestration and enhanced oil recovery
650 of low permeability reservoir in the junggar basin, china. Energy & Fuels
651 28, 3281–3291.

652 Wang, X., Alvarado, V., Swoboda-Colberg, N., Kaszuba, J.P., 2013. Reac-
653 tivity of dolomite in water-saturated supercritical carbon dioxide: Signifi-
654 cance for carbon capture and storage and for enhanced oil and gas recovery.
655 Energy conversion and management 65, 564–573.

Yee, S., Dustin, C., H., H.B., Igor, H., E., D.L., Liwei, Z., Ronghong, L., M., D.R., Wu, Z., Fan, S., R., M.T., 2018. Permeability and mineral composition evolution of primary seal and reservoir rocks in geologic carbon storage conditions. Environmental Engineering Science 35, 391–400. URL: https://www.liebertpub.com/doi/abs/10.1089/ees.2017.0197, doi:10.1089/ees.2017.0197.

Yu, Y., García, B.F., Saraji, S., 2020. Surfactant viscoelasticity as a key parameter to improve supercritical CO_2 foam stability/foamability and performance in porous media. Journal of Non-Newtonian Fluid Mechanics , 104311.

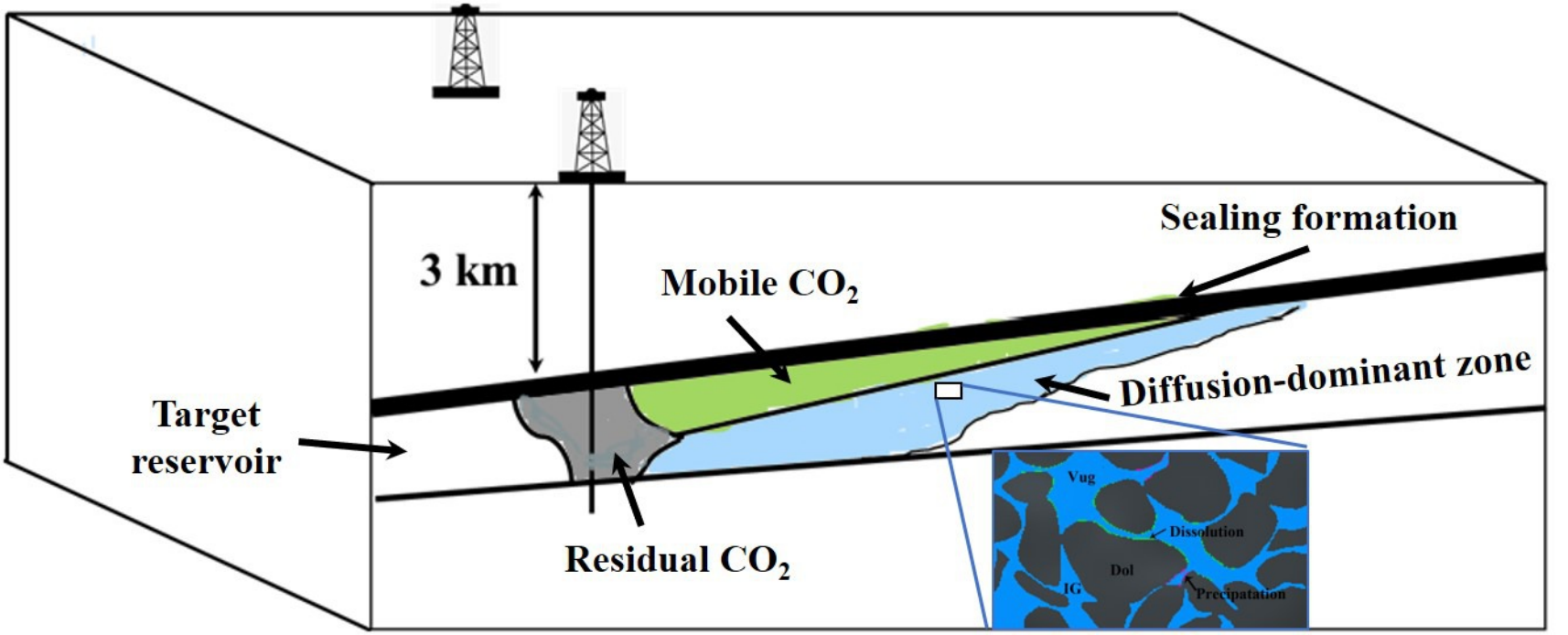
3 km
Sealing formation
Mobile CO_2
Diffusion-dominant zone
Target reservoir
Residual CO_2
Vug
Dissolution
Dol
IG
Precipatation